SCIENTIFIC REPORTS

OPEN

Surface enhanced Raman scattering of monolayer MX$_2$ with metallic nano particles

Duan Zhang[1,2,*], Ye-Cun Wu[2,*], Mei Yang[2], Xiao Liu[2], Cormac Ó Coileáin[2,3,4], Mourad Abid[3], Mohamed Abid[3], Jing-Jing Wang[4], Igor Shvets[4], Hongjun Xu[2,3], Byong Sun Chun[5], Huajun Liu[6] & Han-Chun Wu[2]

Monolayer transition metal dichalcogenides MX$_2$ (M = Mo, W; X = S) exhibit remarkable electronic and optical properties, making them candidates for application within flexible nano-optoelectronics. The ability to achieve a high optical signal, while quantitatively monitoring strain in real-time is the key requirement for applications in flexible sensing and photonics devices. Surface-enhanced Raman scattering (SERS) allows us to achieve both simultaneously. However, the SERS depends crucially on the size and shape of the metallic nanoparticles (NPs), which have a large impact on its detection sensitivity. Here, we investigated the SERS of monolayer MX$_2$, with particular attention paid to the effect of the distribution of the metallic NPs. We show that the SERS depends crucially on the distribution of the metallic NPs and also the phonon mode of the MX$_2$. Moreover, strong coupling between MX$_2$ and metallic NPs, through surface plasmon excitation, results in splitting of the $E'(\Gamma)$ and $A_1'(\Gamma)$ modes and an additional peak becomes apparent. For a WS$_2$-Ag system the intensity of the additional peak increases exponentially with local strain, which opens another interesting window to quantitatively measure the local strain using SERS. Our experimental study may be useful for the application of monolayer MX$_2$ in flexible nano-optoelectronics.

Two dimensional (2D) transition metal dichalcogenides (TMDs) have attracted much attention recently due to their outstanding electronic and optical attributes[1–10]. In contrast with graphene TMDs usually have energy bandgaps, ranging from 1 to 2 eV and typically display a transition from an indirect to direct-bandgap when the thickness is reduced to a monolayer[2,3,11,12] For example, monolayer WS$_2$ has a direct bandgap of 2.1 eV and its bulk state has an indirect bandgap of 1.3 eV[12]. The lack of inversion symmetry of TMDs together with strong spin–orbit coupling may lead to many as yet unforeseen applications[13–15] Recent experimental studies suggest that monolayer WS$_2$ and monolayer MoS$_2$ have carrier mobilities of $\sim$140 cm^2/(V·s) at low temperatures and a high on/off current ratio of 10^6 [16–18]. In particular, intense photoluminescence (PL) has been found in monolayer WS$_2$[19]. These properties suggest that monolayer MX$_2$ has the potential to be candidate within flexible 2D nano-optoelectronics. Mechanical strain is an important parameter in determining the performance of flexible devices[20–27]. It can strongly modify electronic structure and optical properties of 2D semiconductors. For example, a tensile strain exceeding 1% can cause a direct-to-indirect transition of the optical bandgap of monolayer MoS$_2$[25–27]. Thus, to utilize monolayer MX$_2$ within flexible 2D nano-optoelectronics, it is important to find a method to achieve a high optical signal, while quantitatively monitoring strain in real-time. Surface-enhanced Raman scattering (SERS) allows us to achieve both simultaneously. Raman spectroscopy is nondestructive and is widely used to measure the number of atomic layers, and the mechanical and thermal properties of graphene and various inorganic layered materials[28]. Moreover, the optical properties of monolayers such as graphene can be enhanced by surface resonances[29–33], and similarly metals (e.g., Ag and Au) on the surface monolayer MX$_2$ are

[1]Elementary Educational College, Beijing key Laboratory for Nano-Photonics and Nano-Structure, Capital Normal University, Beijing 100048, P. R. China. [2]Key Laboratory of Cluster Science of Ministry of Education, School of Physics, Beijing Institute of Technology, Beijing 100081, P. R. China. [3]KSU-Aramco Center, King Saud University, Riyadh 11451, Saudi Arabia. [4]School of Physics and CRANN, Trinity College, University of Dublin, Dublin 2, Ireland. [5]Division of Industrial Metrology, Korea Research Institute of Standards and Science, Daejeon 305-340, South Korea. [6]Institute of Plasma Physics, Chinese Academy of Sciences, Hefei 230031, P. R. China. *These authors contributed equally to this work. Correspondence and requests for materials should be addressed to H.C.W. (email: wuhc@bit.edu.cn)

known to produce enhancements through surface plasmon resonances[34–36]. However, the SERS depends crucially on the size and shape of metallic nanoparticles (NPs), which have a large impact on its detection sensitivity.

In this paper, we investigated the SERS of monolayer MX_2, with particular attention paid to the effect of the distribution of the metallic NPs. We found that the SERS depends crucially on the distribution of the metallic NPs and also the phonon mode of the MX_2. Strong coupling between the MX_2 and metallic NPs, through surface plasmon excitation, results in splitting of the $E'(\Gamma)$ and $A_1'(\Gamma)$ modes and an additional peak becomes apparent. For the WS_2-Ag system, the intensity of the additional peak increases exponentially with local strain. Our experimental study may be useful for the application of monolayer MX_2 in flexible nano-optoelectronics.

Results

Sample preparation and characterization.
Monolayer MX_2 (M = Mo, W; X = S) can be obtained by the top-down methods, such as mechanical exfoliation[2,37], and chemical exfoliation[38–41], or by bottom up methods, such as transition metal sulfurization or metal oxide sulfurization[42–53], and the decomposition of thiomolybdates[54]. In this work, to achieve large-scale continuous monolayer WS_2 films, a monolayer WO_3 film was first deposited on single crystal sapphire substrate using an e-beam heated WO_3 source in a MBE system (DCA). Figure 1a shows a representative reflection high electron diffraction pattern (RHEED) of an α-Al_2O_3 (0001) substrate after annealing with an oxygen partial pressure of 1×10^{-5} Torr for 2 hours. The observed diffraction pattern of the [0110] crystallographic direction of the α-Al_2O_3 surface shows vertical lattice rods and sharp Kikuchi lines indicating a flat and well-ordered surface. The monolayer WO_3 layer was deposited at a substrate temperature of 400 °C. After growth, the monolayer of WO_3 was annealed at 650 °C with an oxygen partial pressure of 5×10^{-6} Torr for 30 minutes. Figure 1b is the RHEED pattern of a WO_3 monolayer grown on the α-Al_2O_3 substrate after annealing. The sharp lines and diffraction spots originate from monoclinic WO_3 (110) plane. One can see that WO_3 can be epitaxially grown on a sapphire substrate which allows us to precisely control the thickness of WS_2. The chemical composition of the WO_3 was investigated by X-Ray photoelectron spectroscopy (XPS). Figure 1c shows that the W $4f_{7/2}$ and W $4f_{5/2}$ peaks are located at 35.1 eV and 37.2 eV indicating W^{6+} oxidation states. To form WS_2, the sample was removed from the MBE chamber and sulfurized at 700 °C for 15 min in a furnace using 10% H_2 in Argon gas as the carrier. Figure 1d,e show the XPS compositional analysis of monolayer WS_2 grown on a sapphire substrate for the S and W peaks respectively. The peak positions for $W^{4+} 4f_{7/2}$, $W^{4+} 4f_{7/2}$, S $2p_{3/2}$, and S $2p_{1/2}$ are 32.7 eV, 34.7 eV, 162.3 eV, and 163.5 eV respectively. From Fig. 1d,e, we can also estimate that the atomic ratio of W: S is approximately 1: 2. PL spectra were used to further evaluate the thickness of the WS_2 layer (Fig. 1f). A bandgap of ~2 eV was observed indicating the grown WS_2 was monolayer in nature[19]. To produce MoS_2, a procedure similar to that for WS_2 was used. After the growth of monolayer MoO_3 by MBE, the sample was removed from the MBE chamber and sulfurized at 700 °C for 1 min to 2 min in a furnace. The chemical composition of the MoS_2 layer was investigated by XPS (Figures S1a). The Mo $3d_{5/2}$, Mo $3d_{3/2}$, and S 2s peaks have been consistently energy shifted in order to position the peak in the C 1s region at a binding energy (BE) of 284.7 eV. The peak positions for the Mo $3d_{5/2}$, Mo $3d_{3/2}$, and S 2s are 229 eV, 232 eV, and 226 eV respectively, which are consistent with the values for bulk MoS_2. From Figure S1a, we can also estimate that the atomic ratio of Mo: S is approximately 1: 2. Raman spectroscopy was used to further evaluate the quality of the MoS_2 layer. Figure S1b shows high resolution transmission electron microscopy (HRTEM) of a MoS_2 layer. The XPS and HRTEM results indicate the good quality and layered structure of the MoS_2. As the area of the monolayer MX_2 is determined by that of the initial MO_3 monolayer, we developed a convenient technique to produce large-scale monolayer MX_2. The overlaying Ag NPs of different sizes was achieved using E-beam evaporation. The size and the morphology of Ag NPs were characterized by SEM.

SERS at room temperature.
Figure 2a shows a schematic of the experimental set-up. Raman measurements were performed using a Renishaw RM1000 spectrometer with an excitation wavelength of 532 nm. Figure 2b displays the Raman spectra of the monolayer WS_2 without and with Ag NPs on top. Raman modes were assigned by fitting the spectra using a multi-peak Lorentzian approach as displayed in Figure S2. The Raman spectrum of monolayer WS_2 displays an in-plane active mode $E'(\Gamma)$ at 356 cm^{-1} and an out-of-plane mode $A_1'(\Gamma)$ at 417 cm^{-1}. The $2LA(M)$ mode is located at 353 cm^{-1}. Compared with bulk WS_2[55], the frequency of the out-of-plane mode $A_1'(\Gamma)$ is red-shifted from 421 to 417 cm^{-1}. The softening of the $A_1'(\Gamma)$ mode is due to the absence of Van der Waals interactions between the layers. By growing Ag NPs on the top of monolayer WS_2, an increase in the intensity of the Raman active modes is observed, as shown in Fig. 2b. The intensity of the $2LA(M)$ mode is enhanced by a factor of 3. Note, due to the non-uniform distribution of the Ag NPs, the enhancement factor has a variation of approximately 10%. Interestingly, for the out-of-plane $A_1'(\Gamma)$ modes, additional peaks show up (marked with an arrow in Fig. 2b). In the vicinity of the metallic NPs, the electric field will be enhanced due to the collective oscillations of the conduction electrons inside the structure, thus the scattering process is enhanced by a factor of $(E_{local}/E_0)^4$, where E_0 is the strength of the incident E-field and E_{local} is the strength of the local electric field in the presence of the metallic NPs or at the plasmonic hotspots[34–36]. Moreover, the strength of the localized electric field depends on the size, shape and interactions between the isolated NPs. It is also reported that such an enhancement could be maximized if the excitation wavelength was tuned to be close to the surface plasmon resonance wavelength of the metal particles[56–58]. To understand how Ag NPs enhance the Raman signal of our monolayer WS_2, the electric field amplitude cartography was simulated using a Finite Difference Time Domain (FDTD) approach. Figure S3a shows a schematic drawing of the structure used for the simulation. The position and shape of the silver NPs were extracted from SEM images by performing a simple filtering and thresholding processes (Figures S3b and S3c). All the simulations were performed using a mesh size of 0.2 nm in the x, y, and z-directions. Figure 2d shows the simulated electrical field distribution of the real surface with an excitation wavelength of 532 nm. At first glance, the electric field is localized at the Ag NP$-WS_2$ boundary, indicating the enhanced Raman scattering at the Ag NP$-WS_2$ boundary dominates the overall SERS signal which is consistent
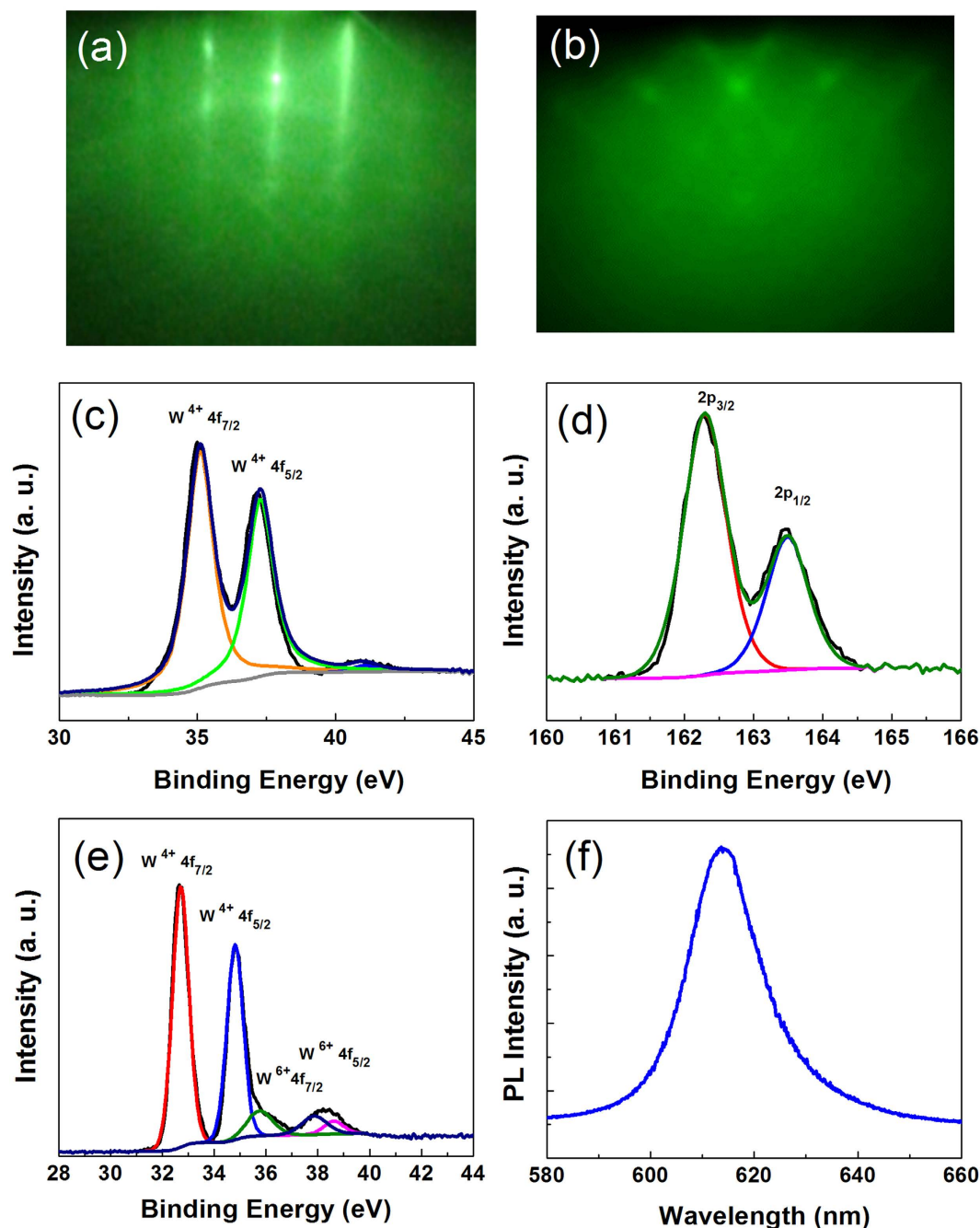
Figure 1. WS₂ characterization. (**a**) RHEED patterns of a sapphire substrate after annealing with oxygen for 2 hours. (**b**) RHEED pattern of monolayer WO₃ grown on a sapphire substrate. (**c**) X-ray photoemission spectroscopy compositional analysis of monolayer WO₃ grown on a sapphire substrate. X-ray photoemission spectroscopy compositional analysis for the S (**d**) and W (**e**) peaks of monolayer WS₂ grown on a sapphire substrate. (**f**) PL spectrum of monolayer WS₂ grown on sapphire substrate.

with other reports[36]. The amplitude of the normalized electric field intensity ($|E_{local}|^2/|E_0|^2$) varies from 3 up to 100, which corresponds to a local enhancement of the Raman scattering of 9 up to 10^4. This heterogeneity is mainly due to the wide range of Ag NP sizes and shapes. Indeed, in the case of a Ag NP with an arbitrary shape, the polarizability of the NP is proportional to $1/(\varepsilon_{WS2} + L_{x,y,z} \cdot (\varepsilon_{WS2} - \varepsilon_{Ag}))$ which is different from the resonance of an ideal sphere ($1/(\varepsilon_{Ag} + 2\varepsilon_{WS2})$), where ε_{Ag} and ε_{WS2} are the dielectric functions of the Ag NP and WS₂ respectively. $L_{x,y,z}$ is the depolarization factor of the NPs in the x, y, and z-directions and $L_x + L_y + L_z = 1$ for an arbitrary shape. Moreover, when the distance between the nanostructures is decreased, strong electromagnetic coupling between the Ag NPs will occur which can further strengthen the electric field at the vicinity of interacting Ag NPs.
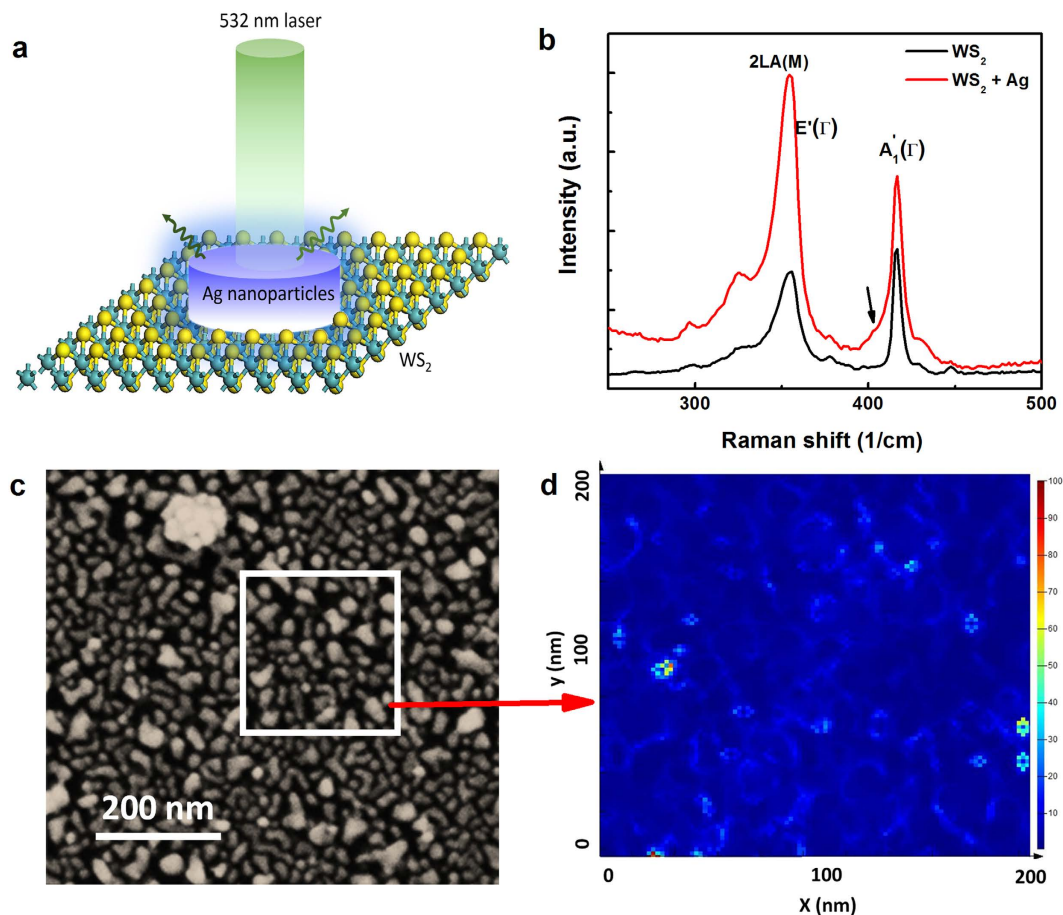
Figure 2. SERS of monolayer WS$_2$ at room temperature. (**a**) Schematic drawing of the experimental setup for the SERS measurements of WS$_2$. (**b**) Raman spectra of monolayer WS$_2$ with (Red) and without (Black) 5 nm nominally thick Ag NPs on top. Arrow indicates the splitting of the $A_1'(\Gamma)$ mode. (**c**) SEM image of 5 nm nominally thick Ag NPs on monolayer WS$_2$. (**d**) Simulated electric field cartography at the surface of the area marked in Fig. 2c with an excitation wavelength of 532 nm.

We observed similar effect in the Ag NP-MoS$_2$ system. Figure 3a displays the Raman spectra of monolayer MoS$_2$ without and with Ag NPs on top. By growing Ag NPs on the top of monolayer MoS$_2$, an increase in the intensity of the Raman active modes is also observed. To clearly demonstrate the SERS effect, Fig. 3c shows the Raman intensity mapping of MoS$_2$ with and without Ag NPs on top. Although a decrease in the intensity can be observed from top to bottom, due to absorbates or contaminants on the surface, the 2D Raman intensity mapping does correlate with the contrast seen in the rectangle in Fig. 3b. Thus, it gives another indication that the enhanced Raman signal is due to the SERS. Moreover, the intensity at the boundary of the bare MoS$_2$ and MoS$_2$/Ag is smaller than that of the MoS$_2$/Ag but larger than that of bare MoS$_2$, thus suggesting observation of the propagation of surface plasmons into the bare monolayer MoS$_2$. Similar to WS$_2$, the $E'(\Gamma)$, and $A_1'(\Gamma)$ modes are split. Clear splitting of the $E'(\Gamma)$ mode was not observed in Fig. 2b for WS$_2$. The reason being that the $E'(\Gamma)$ and $2LA(M)$ modes for WS$_2$ are very close. Moreover, the in-plane mode E_{1g} is activated, which is normally forbidden in the backscattering Raman process.

Thickness dependent SERS. To further investigate the impact of Ag NP distribution on the SERS signal, Fig. 4a shows Raman spectra of monolayer WS$_2$ with different nominal thicknesses of Ag NPs on top. The Raman intensity does depend on the nominal thickness of the Ag NPs and the distribution of the Ag NPs. When the nominal thickness is increased from 1 nm to 10 nm, the morphology of Ag NPs is modified (Figure S4). For a thickness of 1 nm, well separated Ag NPs are present. When the thickness is increased to 5 nm, Ag NPs are separated but elongated and Ag NPs with multiple axes emerge. While for a thickness of 10 nm, it is more like a 10 nm thick non-continuous film on the surface. We define the enhancement factor as the ratio between the Raman intensity (frequency-integrated area under each peak) of a monolayer WS$_2$ covered with Ag NPs and that without Ag NPs. Interestingly, SERS also depends on the phonon mode of the monolayer WS$_2$. The enhancement factors of the $2LA(M)$, $E'(\Gamma)$, and $A_1'(\Gamma)$ modes were 2.6, 3, and 1.5, respectively, for a 5 nm nominal thickness of Ag NPs (Fig. 4b). By increasing the nominal thickness of the Ag NPs from 1 to 5 nm, a clear enhancement of the Raman signal for the $E'(\Gamma)$ and $2LA(M)$ modes is observed, which is followed by a decrease in the enhancement factor
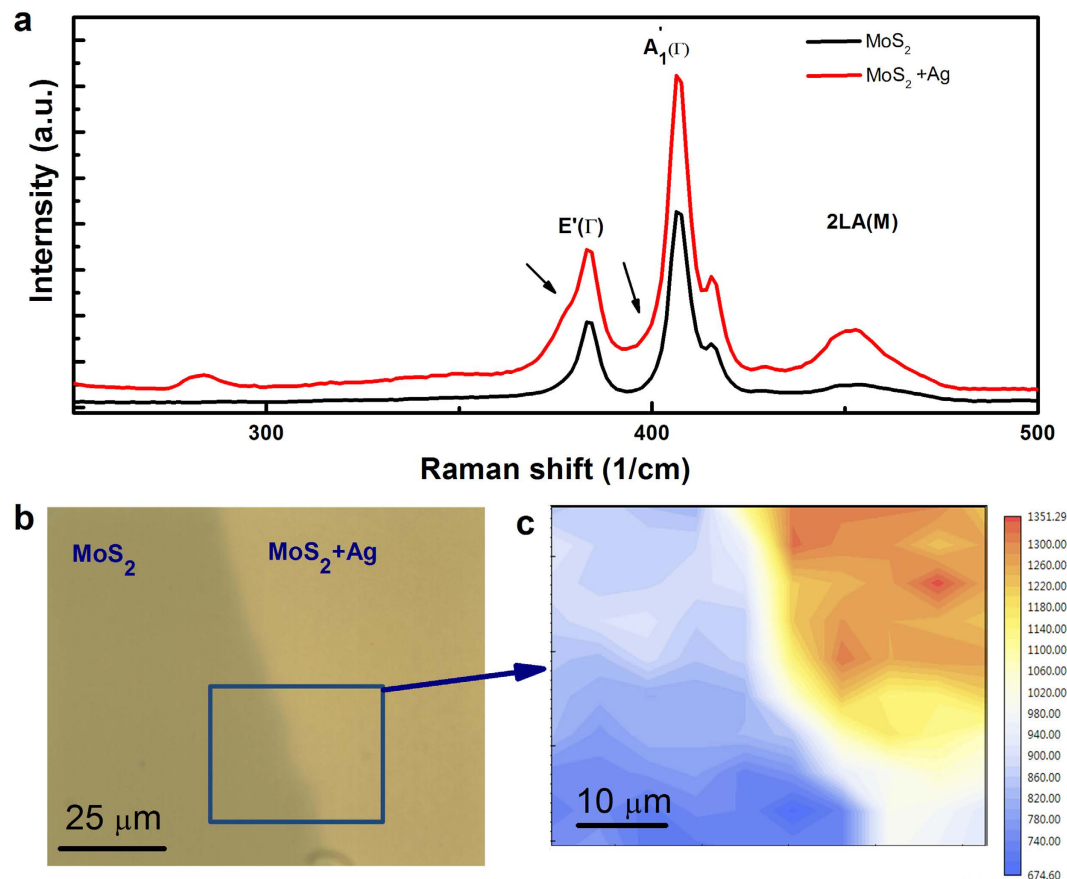
Figure 3. SERS of monolayer MoS$_2$ at room temperature. (**a**) Raman spectra of monolayer MoS$_2$ with (Red) and without (Black) 5 nm nominally thick Ag NPs on top. Arrows indicate the splitting of the $A_1'(\Gamma)$ and $E'(\Gamma)$ modes. (**b**) Optical image of MoS$_2$ with and without Ag NPs on top. (**c**) 2D distribution of Raman intensity corresponding to the rectangle in Fig. 3b.

when the thickness is increased to 10 nm. An explanation for the decrease in the enhancement factor for 10 nm nominally thick Ag NPs can be understood from the Ag morphology. The boundary density for the 10 nm non-continuous film is much less than that for 1 nm or 5 nm Ag NPs which decreases the overall SERS. The enhancement process is also accompanied by a red-shift of the Raman active modes, as shown in Fig. 4a. Interestingly, for out-of-plane $A_1'(\Gamma)$ modes, the enhancement factor is less sensitive to the nominal thickness of the Ag NPs (Fig. 4b) and additional peaks show up at 405 and 432 cm^{-1} (Fig. 4c). It was shown by Wang *et al.* that due to strong surface plasmon excitation, the Raman signal at the boundary of metal-WS$_2$ is dominated by local strain and the out-of-plane $A_1'(\Gamma)$ mode is split[36]. Similar effects can be expected in our Ag NP-WS$_2$ system as the SERS signal is also dominated by the Raman scattering at the Ag NP-WS$_2$ boundary. Moreover, the intensity of the split mode (P1 marked in Fig. 3c) increases linearly with the Ag NP nominal thickness (Figure S5). As the absolute intensity values depend on the laser power, we use I$_{P1}$/I$_{P0}$ where I$_{P1}$ and I$_{P0}$ are the intensities of modes P1 and P0 respectively. The intensity ratio has an error of 8% due to the Lorenztian fittings. To demonstrate it can be used to quantitatively measure the local strain, we plot the intensity of the split peak (P1) as a function of the local strain, where the local strain is quantitated by the relative shift of P0 (Table 1 in supporting information)[59]. In addition, from the error of the relative shift (± 0.1 cm^{-1}), the error for the calculated values of the local strain is approximately ± 0.3%. It is found that the intensity of the split peak increases exponentially with the local strain. Interestingly, the intensity of P2 also follows a similar strain dependence. In our Ag NP-WS$_2$ system, strain is produced by the Ag NP deposition (Fig. 4d). The exponential dependence of the Raman intensity on the local strain opens another interesting window to quantitatively measure the local strain using SERS. It can also explain why the enhancement factor of the $A_1'(\Gamma)$ mode is less than that of the $E'(\Gamma)$ mode.

In conclusion, we investigated SERS for monolayer MX$_2$, paying particular attention to the effect of the distribution of the metallic NPs. We show that the SERS depends crucially on the distribution of the Ag NPs and also the phonon modes of the MX$_2$. Moreover, strong coupling between the MX$_2$ and the Ag NPs through surface plasmon excitation results in splitting of the $A_1'(\Gamma)$ mode and additional peaks are manifested. The intensity of the additional peak increases exponentially with local strain, which opens another interesting window into quantitatively measuring the local strain through SERS.
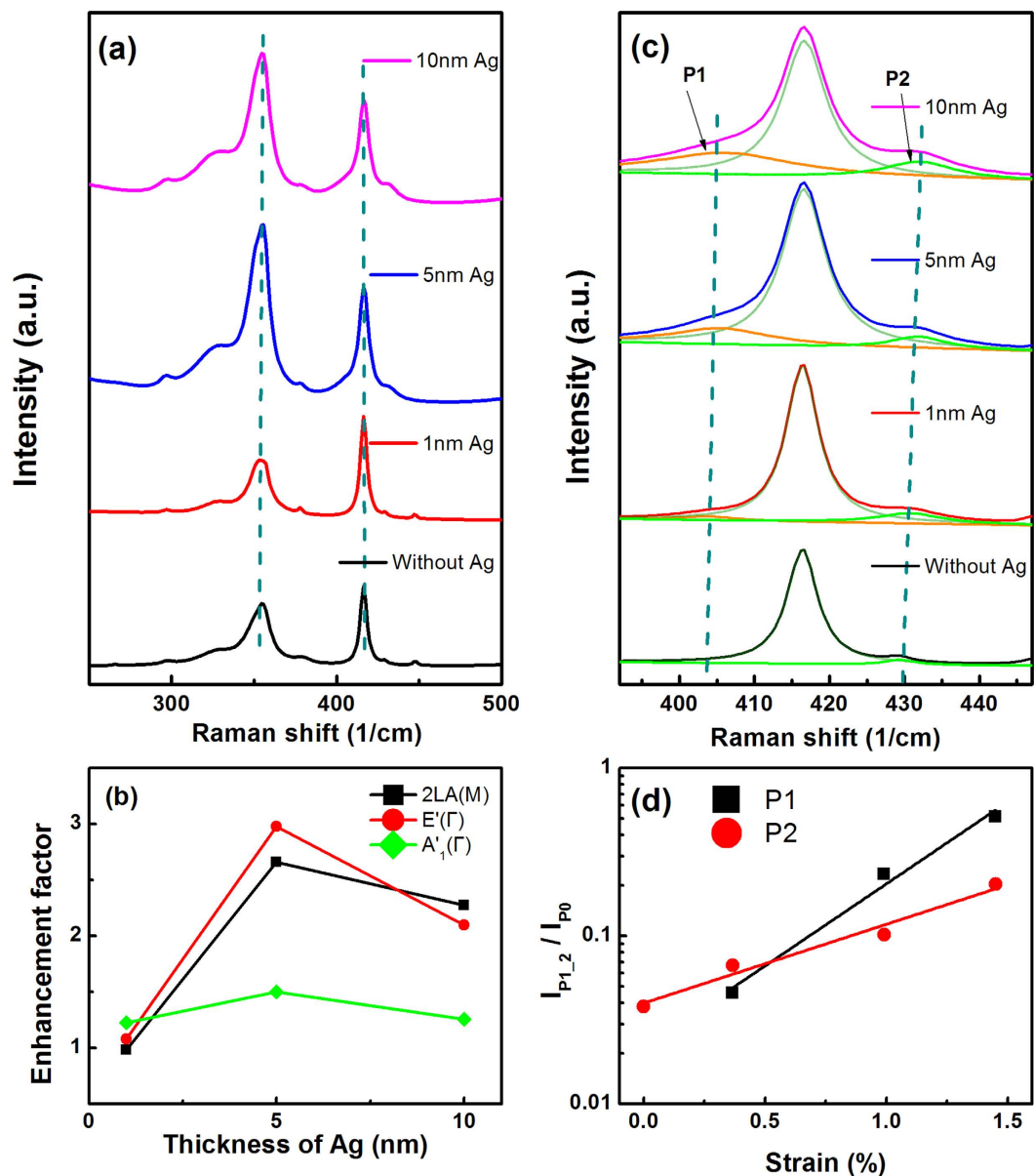
Figure 4. Thickness dependent SERS of monolayer WS2 and splitting of $A_1'(\Gamma)$ mode at room temperature.
(**a**) Raman spectra of monolayer WS_2 with different thickness Ag NPs on top. (**b**) Enhancement factors as a function of the Ag NP thickness. (**c**) Raman splitting of the $A_1'(\Gamma)$ mode with different thickness Ag NPs on top of it. (**d**) I_{P1}/I_{P0} and I_{P2}/I_{P0} as a function of the Ag NP thickness induced strain.

Methods

Monolayer MX$_2$ growth and characterization. To achieve large-scale continuous monolayer MX_2 films, a monolayer MO_3 film was first deposited on single crystal sapphire substrate using an e-beam heated MO_3 source in a MBE system (DCA). Reflection high electron diffraction (RHEED) was used to monitor and establish growth mode. After growth, the monolayer of MO_3 was annealed with an oxygen partial pressure of 5×10^{-6} Torr for 30 minutes. To form MX_2, the sample was removed from the MBE chamber and sulfurized in a furnace using 10% H_2 in Argon gas as the carrier. The quality of the sample was investigated by X-ray photoemission spectroscopy (XPS), Raman spectroscopy, high resolution transmission electron microscopy (HRTEM), and PL spectroscopy indicating the high quality of the monolayer MX_2.

References

1. Wang, Q., Kalantar-Zadeh, K., Kis, A., Coleman, J. & Strano, M. Electronics and optoelectronics of two-dimensional transition metal dichalcogenides. *Nat. Nanotech.* **7,** 699–712 (2012).
2. Mak, K., Lee, C., Hone, J., Shan, J. & Heinz, T. Atomically Thin MoS$_2$: A New Direct-Gap Semiconductor. *Phys. Rev. Lett.* **105,** 136805 (2010).
3. Sobhani, A. *et al.* Enhancing the photocurrent and photoluminescence of single crystal monolayer MoS2 with resonant plasmonic nanoshells. *Appl. Phys. Lett.* **104,** 031112 (2014).

4. Radisavljevic, B., Radenovic, A., Brivio, J., Giacometti, V. & Kis, A. Single-layer MoS$_2$ transistors. *Nat. Nanotech.* **6,** 147–150 (2011).
5. Xiao, D., Liu, G., Feng, W., Xu, X. & Yao, W. Coupled Spin and Valley Physics in Monolayers of MoS$_2$ and Other Group-VI Dichalcogenides. *Phys. Rev. Lett.* **108,** 196802 (2012).
6. Jones, A. *et al.* Optical generation of excitonic valley coherence in monolayer WSe$_2$. *Nat. Nanotech.* **8,** 634–638 (2013).
7. Cao, T. *et al.* Valley-selective circular dichroism of monolayer molybdenum disulphide. *Nat. Commun.* **3,** 887 (2012).
8. Mak, K., He, K., Shan, J. & Heinz, T. Control of valley polarization in monolayer MoS$_2$ by optical helicity. *Nat. Nanotech.* **7,** 494–498 (2012).
9. Mak, K., McGill, K., Park, J. & McEuen, P. The valley Hall effect in MoS$_2$ transistors. *Science* **344,** 1489–1492 (2014).
10. Zhang, Y., Oka, T., Suzuki, R., Ye, J. & Iwasa, Y. Electrically Switchable Chiral Light-Emitting Transistor. *Science* **344,** 725–728 (2014).
11. Zhao, W. *et al.* Evolution of Electronic Structure in Atomically Thin Sheets of WS$_2$ and WSe$_2$. *ACS Nano* **7,** 791–797 (2013).
12. Kuc, A., Zibouche, N. & Heine, T. Influence of quantum confinement on the electronic structure of the transition metal sulfide TS$_2$. *Phys. Rev. B* **83,** 245213 (2011).
13. Xiao, D., Liu, G., Feng, W., Xu, X. & Yao, W. Coupled Spin and Valley Physics in Monolayers of MoS$_2$ and Other Group-VI Dichalcogenides. *Phys. Rev. Lett.* **108,** 196802 (2012).
14. Rycerz, A., Tworzydło, J. & Beenakker, C. Valley filter and valley valve in graphene. *Nat. Phys.* **3,** 172–175 (2007).
15. Xiao, D., Yao, W. & Niu, Q. Valley-Contrasting Physics in Graphene: Magnetic Moment and Topological Transport. *Phys. Rev. Lett.* **99,** 236809 (2007).
16. Withers, F., Bointon, T., Hudson, D., Craciun, M. & Russo, S. Electron transport of WS$_2$ transistors in a hexagonal boron nitride dielectric environment. *Sci. Rep.* **4,** 4967 (2014).
17. Liu, X. *et al.* High Performance Field-Effect Transistor Based on Multilayer Tungsten Disulfide. *ACS Nano* **8,** 10396–10402 (2014).
18. Ovchinnikov, D., Allain, A., Huang, Y. S., Dumcenco, D. & Kis, A. Electrical Transport Properties of Single-Layer WS$_2$. *ACS Nano* **8,** 8174–8181 (2014).
19. Peimyoo, N. *et al.* Nonblinking, Intense Two-Dimensional Light Emitter: Monolayer WS$_2$ Triangles. *ACS Nano* **7,** 10985–10994 (2013).
20. Conley, H. *et al.* Bandgap Engineering of Strained Monolayer and Bilayer MoS$_2$. *Nano Lett.* **13,** 3626–3630 (2013).
21. Zhu, C. *et al.* Strain tuning of optical emission energy and polarization in monolayer and bilayer MoS$_2$. *Phys. Rev. B* **88,** 121301 (2013).
22. Pu, J. *et al.* Highly Flexible MoS$_2$ Thin-Film Transistors with Ion Gel Dielectrics. *Nano Lett.* **12,** 4013–4017 (2012).
23. Chang, H. *et al.* High-Performance, Highly Bendable MoS$_2$ Transistors with High-K Dielectrics for Flexible Low-Power Systems. *ACS Nano* **7,** 5446–5452 (2013).
24. Yoon, J. *et al.* Flexible Electronics: Highly Flexible and Transparent Multilayer MoS$_2$ Transistors with Graphene Electrodes. *Small* **9,** 3185–3185 (2013).
25. Lu, P., Wu, X., Guo, W. & Zeng, X. Strain-dependent electronic and magnetic properties of MoS$_2$ monolayer, bilayer, nanoribbons and nanotubes. *Phys. Chem. Chem. Phys.* **14,** 13035 (2012).
26. Pan, H. & Zhang, Y. Tuning the Electronic and Magnetic Properties of MoS$_2$ Nanoribbons by Strain Engineering. *J. Phys. Chem. C* **116,** 11752–11757 (2012).
27. Shi, H., Pan, H., Zhang, Y. & Yakobson, B. Quasiparticle band structures and optical properties of strained monolayer MoS$_2$ and WS$_2$. *Phys. Rev. B* **87,** 155304 (2013).
28. Calizo, I., Balandin, A., Bao, W., Miao, F. & Lau, C. Temperature Dependence of the Raman Spectra of Graphene and Graphene Multilayers. *Nano Lett.* **7,** 2645–2649 (2007).
29. Kim, N., Oh, M. K., Park, S., Kim, S. K. & Hong, B. H. Effect of Gold Substrates on the Raman Spectra of Graphene. *Bull. Korean Chem. Soc.* **31,** 999–1003 (2010).
30. Sidorov, A. N., Sławiński, G. W., Jayatissa, A. H. & Zamborini, F. P. Sumanasekera G.U. A surface-enhanced Raman spectroscopy study of thin graphene sheets functionalized with gold and silver nanostructures by seed-mediated growth. *Carbon* **50,** 699 (2012).
31. Wang, P. *et al.* Giant Optical Response from Graphene–Plasmonic System. *Acs Nano* **6,** 6244 (2012).
32. Khorasaninejad, M. *et al.* Highly Enhanced Raman Scattering of Graphene using Plasmonic Nano-Structure. *Sci. Rep.* **3,** 2936, 2013
33. Kalbac, M., Vales, V. & Vejpravova, J. The effect of a thin gold layer on graphene: a Raman spectroscopy study. *RSC Adv.* **4,** 60929–60935 (2014).
34. Xu, H., Aizpurua, J., Käll, M. & Apell, P. Electromagnetic contributions to single-molecule sensitivity in surface-enhanced Raman scattering. *Phys. Rev. E* **62,** 4318–4324 (2000).
35. Le Ru, E. & Etchegoin, P. Quantifying SERS enhancements. *MRS Bull.* **38,** 631–640 (2013).
36. Sun, Y. *et al.* Probing Local Strain at MX2 –Metal Boundaries with Surface Plasmon-Enhanced Raman Scattering. *Nano Lett.* **14,** 5329–5334 (2014).
37. Novoselov, K. Electric Field Effect in Atomically Thin Carbon Films. *Science* **306,** 666–669 (2004).
38. Coleman, J. *et al.* Two-Dimensional Nanosheets Produced by Liquid Exfoliation of Layered Materials. *Science* **331,** 568–571 (2011).
39. Paton, K. *et al.* Scalable production of large quantities of defect-free few-layer graphene by shear exfoliation in liquids. *Nat. Mater.* **13,** 624–630 (2014).
40. Joensen, P., Frindt, R. & Morrison, S. Single-layer MoS2. *Mater. Res. Bull.* **21,** 457–461 (1986).
41. Eda, G. *et al.* Photoluminescence from Chemically Exfoliated MoS$_2$. *Nano Lett.* **11,** 5111–5116 (2011).
42. Lee, K., Gatensby, R., McEvoy, N., Hallam, T. & Duesberg, G. High-Performance Sensors Based on Molybdenum Disulfide Thin Films. *Adv. Mater.* **25,** 6699–6702 (2013).
43. Zhan, Y., Liu, Z., Najmaei, S., Ajayan, P. & Lou, J. Large-Area Vapor-Phase Growth and Characterization of MoS2 Atomic Layers on a SiO$_2$ Substrate. *Small* **8,** 966–971 (2012).
44. Kong, D. *et al.* Synthesis of MoS$_2$ and MoSe$_2$ Films with Vertically Aligned Layers. *Nano Lett.* **13,** 1341–1347 (2013).
45. Gatensby, R. *et al.* Controlled synthesis of transition metal dichalcogenide thin films for electronic applications. *Appl. Surf. Sci.* **297,** 139–146 (2014).
46. Gutiérrez, H. *et al.* Extraordinary Room-Temperature Photoluminescence in Triangular WS$_2$ Monolayers. *Nano Lett.* **13,** 3447–3454 (2013).
47. Song, J. *et al.* Layer-Controlled, Wafer-Scale, and Conformal Synthesis of Tungsten Disulfide Nanosheets Using Atomic Layer Deposition. *ACS Nano* **7,** 11333–11340 (2013).
48. Orofeo, C., Suzuki, S., Sekine, Y. & Hibino, H. Scalable synthesis of layer-controlled WS$_2$ and MoS$_2$ sheets by sulfurization of thin metal films. *Appl. Phys. Lett.* **105,** 083112 (2014).
49. Elías, A. *et al.* Controlled Synthesis and Transfer of Large-Area WS$_2$ Sheets: From Single Layer to Few Layers. *ACS Nano* **7,** 5235–5242 (2013).
50. Jung, Y. *et al.* Metal Seed Layer Thickness-induced transition from vertical to horizontal growth of MoS$_2$ and WS$_2$. *Nano Lett.* **14,** 6842–6849 (2014).
51. Morrish, R., Haak, T. & Wolden, C. Low-Temperature Synthesis of n -Type WS$_2$ Thin Films via H$_2$S Plasma Sulfurization of WO$_3$. *Chem. Mater.* **26,** 3986–3992 (2014).
52. Yun, S. *et al.* Synthesis of Centimeter-Scale Monolayer Tungsten Disulfide Film on Gold Foils. *ACS Nano* **9,** 5510–5519 (2015).
53. O'Brien, M. *et al.* Plasma assisted synthesis of WS$_2$ for gas sensing applications. *Chem. Phys. Lett.* **615,** 6–10 (2014).

54. Kang, K. *et al.* High-mobility three-atom-thick semiconducting films with wafer-scale homogeneity. *Nature* **520,** 656–660 (2015).
55. Zhang, X. *et al.* Phonon and Raman scattering of two-dimensional transition metal dichalcogenides from monolayer, multilayer to bulk material. *Chem. Soc. Rev.* **44,** 2757–2785 (2015).
56. Niu, J. *et al.* Study of electromagnetic enhancement for surface enhanced Raman spectroscopy of SiC graphene. *Appl. Phys Lett.* **100,** 191601 (2012).
57. Singha, S. S., Nandi, D. & Singha, A. Tuning the photoluminescence and ultrasensitive trace detection properties of few-layer MoS_2 by decoration with gold nanoparticles. *RSC Adv*. **5,** 24188, (2015).
58. Ling, X. *et al.* Raman Enhancement Effect on Two-Dimensional Layered Materials: Graphene, h-BN and MoS_2. *Nano Lett.* **14,** 6 3033 (2014).
59. Wang, Y. *et al.* Strain-induced direct–indirect bandgap transition and phonon modulation in monolayer WS_2. *Nano Resear*. **8,** 2562–2572 (2015).

Acknowledgements

Author Contributions

H.-C.W. supervised the project and led the overall effort. D.Z., Y.-C.W., M.Y. and X.L. carried out the Raman measurements. C.Ó.C., M.A. and I.S. grew the sample. B.S.C. performed TEM characterization. M.A. performed the FDTD simulation. D.Z., Y.-C.W., J.-J.W., H.X., H.L. and H.-C.W. analyzed the data. H.-C.W. wrote the paper. All authors discussed the results and commented on the manuscript.

Additional Information

Supplementary information accompanies this paper at http://www.nature.com/srep

Competing financial interests: The authors declare no competing financial interests.

How to cite this article: Zhang, D. *et al.* Surface enhanced Raman scattering of monolayer MX2 with metallic nano particles. *Sci. Rep.* **6**, 30320; doi: 10.1038/srep30320 (2016).